Engineering Fracture Mechanics 214 (2019) 149–163

Contents lists available at ScienceDirect

Engineering Fracture Mechanics

journal homepage: www.elsevier.com/locate/engfracmech

In-situ SEM investigation on fatigue behaviors of additive manufactured Al-Si10-Mg alloy at elevated temperature

Zhen Wang[a], Wenwang Wu[b,⁎], Guian Qian[c], Lijuan Sun[c], Xide Li[a,⁎], José A.F.O. Correia[d]

[a] Department of Engineering Mechanics, Tsinghua University, Beijing, China
[b] Institute of Advanced Structure &Technology, Beijing Institute of Technology, Beijing 100081, China
[c] State Key Laboratory for Nonlinear Mechanics (LNM), Institute of Mechanics, Chinese Academy of Sciences, Beijing, China
[d] Faculty of Engineering, University of Porto (FEUP), R. Dr. Roberto Frias, 4200-465 Porto, Portugal

ARTICLE INFO

Keywords:
In-situ SEM
Fatigue
Crack propagation
High temperature
Computer tomography

ABSTRACT

In-situ high temperature measurement in a scanning electron microscopy (SEM) environment is an important technique for exploring the microstructure evolution and crack propagation within refractory materials and other advanced alloys. In this paper, in-situ tensile fatigue experiments under SEM environment at room temperature and elevated temperature are performed for studying the fatigue performance and crack propagation process of selective laser melting (SLM) additive manufactured Al-Si10-Mg materials. Firstly, in-situ SLM additive manufactured Al-Si10-Mg fatigue tensile samples are prepared, and micro-CT are employed for the characterization of void defects within SLM additive manufactured Al-Si10-Mg with different laser scanning speeds and laser energy; Secondly, in-situ fatigue experiments are carried out under SEM environment at 25 °C, 100 °C, 200 °C, 300 °C, 400 °C, 500 °C and 600 °C, respectively. The fatigue mechanical behaviors, microstructure evolution and crack propagations of as-fabricated Al-Si10-Mg samples are characterized. Finally, micro-CT tomography 3D imaging techniques are employed for exploring the link between SLM defects and fatigue performances.

1. Introduction

In contrast to traditional metal manufacturing techniques, metal additive manufacturing (AM) is becoming a disruptive technology capable of revolutionizing the way that products are designed, and demonstrates superior manufacturing efficiency and economic advantages for advanced lightweight industrial components with unlimited arbitrary topological layouts and complex internal microstructures, thus researches and developments on AM techniques are widely accepted in biomedical, aerospace, automotive, marine and offshore industrial sections. As opposed to traditional subtractive manufacturing technologies, metal additive manufacturing (AM) is the process of fabricating optimized devices with complex internal structures through layer-by-layer build-up of parts, and the mechanical properties of as-fabrication industrial components are comparable to that of wrought materials. Despite the huge progress in recent years in metal AM technologies, there remain some production issues which undermine the mechanical integrity of as-fabricated industrial components, including unwanted porosity from incorrect processing parameters or build conditions, surface roughness or other surface imperfections, residual stresses and resultant deformation caused by the complex thermal history, and anisotropic mechanical properties, which are closely related to laser speed, laser energy, scanning path strategy and

---

⁎ Corresponding authors.
E-mail addresses: wuwenwang@bit.edu.cn (W. Wu), lixide@tsinghua.edu.cn (X. Li).

https://doi.org/10.1016/j.engfracmech.2019.03.040
Received 29 January 2019; Received in revised form 13 March 2019; Accepted 25 March 2019
Available online 15 April 2019
0013-7944/ © 2019 The Authors. Published by Elsevier Ltd. This is an open access article under the CC BY-NC-ND license (http://creativecommons.org/licenses/BY-NC-ND/4.0/).

powder thickness, etc. [1,2]. These manufacturing process induced imperfections which can be amplified due to the complex nature of the designs. Industrial applications of additive manufactured industrial components are still limited due to the degradation of mechanical integrity under complex static and dynamic external mechanical loading environment. Moreover, AM process parameters, thermal history, solidification, and resultant microstructure of the AM materials are closely related to the mechanical integrity of AM parts, such as stiffness, strength, ductility, corrosion, and fatigue resistances [3,4]. Compared to the static strength and stiffness, investigations on the dynamic performances of AM materials and structures are quite limited, where as-built defects and surface roughness act as sources of crack formation and stress concentration. In-depth and comprehensive investigations on the relations between fabrication process, microstructure and mechanical properties of additive manufactured metals and alloys are mandatory for improving the static and dynamic mechanical integrity of as-fabricated AM components. Considered as promising lightweight structural materials for aerospace and automobile industrial sections, the static and dynamic mechanical performances of additive manufactured Al-Si10-Mg alloys are widely explored in the recent years, such as strength, stiffness, impact energy absorption, etc. However, the fatigue performances and failure mechanisms under various types of harsh loading conditions are not yet well understood, which is one of the most important factors impeding the industrial applications of additive manufactured Al-Si10-Mg alloys. Thus, the relations between manufacturing process, surface and internal defect formation mechanisms, residual stress control and fatigue performances of additive manufactured Al-Si10-Mg alloys should be investigated systematically.

Making use of statistical methods and energy density model, Read et al. [5] investigated the influences of SLM process parameters on the porosity development within as-built Al-Si10-Mg alloy samples, including laser power, scan speed, scan spacing, and island size, etc. Buchbinder et al. [6] investigated the effects of build-up direction, laser scanning velocity and scanning spacing, and metal powder layer thickness on the tensile strength of SLM additive manufactured Al alloys systematically. In addition, the effects of post-treatment of additive manufacturing materials on fatigue performance are also critical, including thermal treatment and surface treatment. Maamoun et al. [7] investigated the effects of thermal post-processing on the microstructure homogeneity of additive manufactured Al-Si10-Mg parts manufactured with recycled powder, and explored the relations between residual stress, hardness, annealing temperature, and annealing time period. Brandl et al. [8] investigated the relations among manufacturing process parameters, microstructure, high cycle fatigue (HCF) and fracture behavior of SLM additive manufactured Al-Si10-Mg samples. It was found that the post heat treatment had the most considerable effect and the building direction had the least considerable effect on the fatigue resistance. The as-built materials usually have large roughness, which affects the fatigue performance and aesthetics of the material. Commonly, surface treatment techniques are used to decrease roughness, including sand blasting [9] chemical etching [10], mechanical polishing [11], electrochemical polishing [12], etc. Bagherifard et al. [9] investigated the individual and synergetic effects of various types of post treatments on the fatigue strength of mechanical properties of SLM fabricated Al-Si10-Mg specimens, and found that appropriate post treatments could significantly enhance the fatigue performance of SLM specimens. Aboulkhair et al. [10] investigated effects of surface quality and heat treatment on the fatigue performance of SLM Al-Si10-Mg and found that specially-tailored heat treatment could increase the material's ductility and refined the microstructure of as-built samples with good fatigue crack propagation resistance. Brandao et al. [11] investigated the influence of building directions, platform temperature, powder layer thickness, surface finish and heat treatment on the fatigue properties of the AM Al-Si10-Mg specimens, and the correlation between process parameters and characteristics of defects population was studied through X-ray tomography, thus determining the fatigue resistance and fatigue crack propagation path. Obviously, these treatment methods are used by different researchers. However, the first three methods are time consuming, and difficult to apply to complex geometric components. Electrochemical polishing techniques could solve this problem [12]. Unfortunately, pre-optimized parameters of surface treatment are often difficult to determine.

As a powerful and frequently employed tool for surface defect and microstructure characterization for material fatigue investigation, the SEM allows contrasted images to be acquired with sub-micrometer spatial resolution over the surface of metals. In recent decades, in-situ mechanical tests within SEM chambers are performed for studying the mechanical behaviors and microstructure evolution process of materials under room and elevated temperatures during static and dynamic loading process [13]. Han [14] performed SEM observation of slip lines and crack initiations during the fretting fatigue process of nickel-based single alloys, and a crystal plasticity constitutive model considering cyclic hardening effect was employed for crystal plasticity finite element simulation, where predicted slip lines, crack initiation locations and orientations were in good agreements with observations. The effect of partial recrystallization on low cycle fatigue (LCF) life of directionally solidified DZ4 superalloy was studied in-situ SEM, and three typical recrystallization microstructures were investigated [15]. In-situ low cycle fatigue test of nickel-based single crystal superalloy up to 800 °C was performed, where Al_2O_3 nano-scale particles were used as high temperature speckle patterns for digital image correlation based displacement field analysis [16]. Small fatigue crack growth behaviors of a nickel-based single crystal were studied through in-situ SEM observation, and two different crack propagation modes were identified, namely non-crystallographic propagation mode at relatively low temperature region, and crack propagation preferentially along crystallographic slip systems at elevated temperature region [17]. Fatigue crack opening displacements for a small contained fatigue crack in the ultra-fine grain size aluminium alloy (IN 9052) were investigated by using in-situ SEM observation technique [18]. Making use of sequential SEM images, strain localization during fatigue crack initiation and early crack propagation in an advanced Ni-based superalloy were investigated using digital image correlation (DIC) methods [19]. Overall process of crack nucleation and propagation of Mo-based high entropy alloy (HEA) was investigated based on in-situ SEM observations, and multiple deformation mechanisms were recognized in the crack tip plastic zone, involving both slip and twinning [20]. Localized deformation, crack initiation and propagation behavior of titanium alloy were investigated through the in-situ SEM test and electron backscatter diffraction (EBSD) characterization [21]. Crack initiation, propagation, fracture, fatigue life, and the mechanical response of micro-cantilever samples of a Ni-based superalloy (Rene-N5) under different cyclic strain amplitudes were investigated using in-situ SEM high frequency fatigue testing methodology [22]. In-situ SEM/EBSD fatigue tests of austenite and ferrite in duplex stainless steels were performed for studying the slip activities and propagation of the fatigue cracks [23]. The fatigue crack initiation and propagation behaviors of a non-notch high strength 2524 aluminum alloy were investigated using in-situ SEM fatigue test at room temperature, and the main crack was found propagating along either slip bands in a shearing mechanism, or along the direction of micro-crack ahead of crack tip in a crack-linking mechanism [24]. In-situ SEM fatigue testing was proposed for investigating the fatigue crack growth mechanisms within one cyclic loading under plane stress conditions [25]. Crack closure and opening behavior of physically short fatigue crack tip were investigated using the in-situ SEM fatigue test, and the contribution of the gradient crack closure zone on the physically short fatigue crack growth behavior was evaluated by using the modified partial crack closure model [26].

The fatigue performances and crack propagation resistances of alloy materials and structures are closely related to the underlying microstructure evolution and defects interactions [27–37]. X-ray computed tomography is a method of forming 3D representations of the internal microstructures by taking many X-ray images around an axis of rotation and using algorithms to reconstruct a 3D model [38–40]. Most of defects formed within additive manufactured parts can be attributed to non-optimal build conditions, powder particle shapes, the particle size distribution, oxidation level, humidity, and static charge, which all can influence the flow ability of the powder, packing density, and homogeneity of the deposited powder layer, ultimately impact on the process and resulting porosity [41–47]. Micro computed tomography (CT) technique allows non-destructive insights into the surface roughness and internal defects spatial and size distribution of additive manufactured parts [48]. Plessis et al. [49] proposed a method for accurate dimensional accuracy, surface roughness and average density from CT information. Combing X-ray CT and uniaxial tensile fatigue test, Tammas et al. [50] investigated the relation between porosity and fatigue lifetime of electron beam melting (EBM) manufactured samples, and concluded that the actual initiating defect within the top 3% of defects in size were most harmful.

In this paper, in-situ tensile fatigue experiments under SEM environment are performed for studying the fatigue performances and crack propagation process of SLM additive manufactured Al-Si10-Mg materials at room temperature and elevated temperature. Firstly, SLM additive manufactured Al-Si10-Mg tensile samples are prepared for quasi-static mechanical properties testing, and micro-CT are employed for characterization of void defects within SLM additive manufactured Al-Si10-Mg with difference laser scanning speed; Secondly, fatigue tensile samples with side notch are fabricated with SLM technique at specific laser energy and scanning speed; Thirdly, in-situ fatigue experiments are carried out under SEM environment at 25 °C, 100 °C, 200 °C, 300 °C, 400 °C, 500 °C and 600 °C, respectively. The fatigue mechanical behaviors, microstructure evolution and crack propagations are characterized. Finally, micro-CT characterization is employed for exploring the link between SLM defects and fatigue performances.

2. Sample preparation and in-situ fatigue test procedures

The Al-Si10-Mg materials based fatigue test samples used for this study were fabricated using an EOS M M290 (constructed by EOS GmbH, Germany) machine, a selective laser melting system from SLM Solutions GmbH. Raw material powder was obtained from EOS GmbH, certified with particle sizes ranging from 18 to 58 µm. The chemical composition by weight percentage (wt%) is shown in Table 1. The build chamber was backfilled with argon gas, while powder melting and fusion was performed using 370 W laser with spot size 200 μm. The fatigue test specimens with U-shaped edge notch located at the center of the gauge section was specially designed for crack formation, with corresponding geometrical layout shown in Fig. 1, and all the samples in this study were fabricated along horizontal direction and constructed layer-by-layer scanning. During the manufacturing process, constant laser energy at power $P_L = 370$ W was used, and the designed samples are supported on a plate heated to 220 °C, and three different printing speeds were adopted, 700 mm/s, 1000 mm/s and 1300 mm/s with powder layer thickness of 0.03 mm, respectively. To relieve residual stresses generated by the fabrication process, thermal stress relieving was performed on these specimens at 300 °C for 2 h, prior to removing specimens from the support structures. Afterwards, these fabricated samples naturally cooled down to the room temperature, and were harvested for in-situ SEM fatigue experiments. Finally, three types of specimens were harvested, and micro-CT 3D tomography imaging with ZEISS METROTOM at accelerating voltage 225 kV was performed for checking the porosity percentages formed within these as-fabricated samples, and the fabricated samples and porosity results were shown in Fig. 2 and Table 2, respectively. In order to achieve a mirror-like surface, these specimens were mechanical polished using SiC paper with grit scales of 400, 800, 1500, 2000, 5000 and 7000, respectively, and finally with 0.5 µm liquid pastes using ultrasonic vibration polishing technique. The final harvested specimens had a thickness of 0.5 mm.

3. In-situ fatigue performances of SLM samples

3.1. In-situ SEM fatigue test at elevated temperature

In-situ high temperature tensile fatigue tests were conducted in the chamber of the SEM (SS-550, Shimadzu, Japan), in which the loading system was controlled using an electro hydraulic servo system and the maximum loading capacity of the in-situ tensile fatigue

Table 1
Chemical composition of the additive manufactured Al-Si10-Mg alloys (wt%).

Element	Cu	Fe	Mg	Mn	Si	Ti	Zn	Al
Content	< 0.05	< 0.55	0.2–0.45	< 0.45	9.0–11.0	< 0.15	< 0.10	Balance

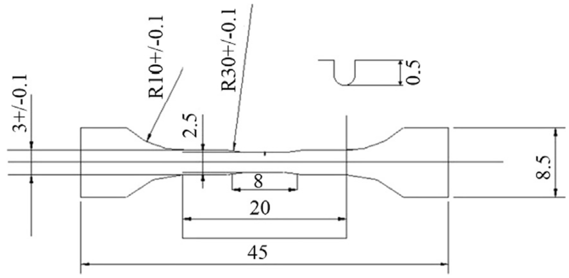

Fig. 1. Geometry of the Al-Si10-Mgspecimen used in fatigue test (unit: mm).

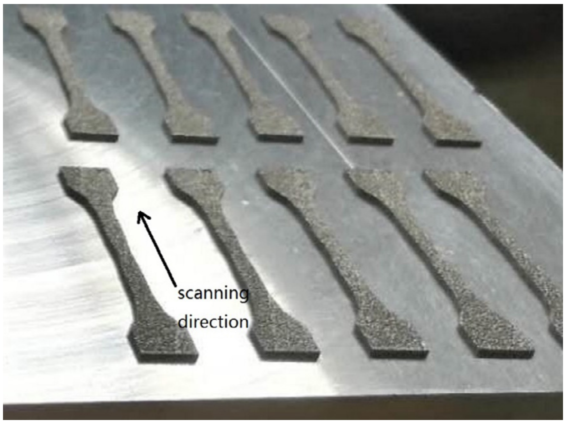

Fig. 2. As printed harvestedAl-Si10-Mg samples for in-situ SEM fatigue experiments.

Table 2
Porosity of Al-Si10-Mg samples under different SLM laser speeds.

Scanning speed (mm/s)	Porosity rate						
700	2.10%	3.21%	2.56%	4.02%	3.02%	2.45%	2.28%
1000	0.68%	0.83%	0.51%	0.68%	0.92%	0.45%	0.65%
1300	0.77%	0.93%	0.67%	0.65%	0.87%	0.74%	0.89%

machine was 1.0 kN, with maximum frequency of 10 Hz, as shown in Fig. 3. The specimen was heated by means of thermal radiation inside a vacuum chamber. The heating system could heat the specimen up to 800 °C with temperature control accuracy of ± 2 °C [16]. In the following, fatigue experiments of Al-Si10-Mg samples were performed at 25 °C, 100 °C, 200 °C, 300 °C, 400 °C, 500 °C and 600 °C, respectively. All fatigue experiments were carried out with sinusoidal waveform loading mode at frequency 5.0 Hz. The peak stress was 160 MPa at the stress ratio $R = 0.2$ by using load controlled mode, as shown in Fig. 4. The process of the crack initiation and propagation were recorded by SEM scanning at interrupted stop state after different cycles during fatigue tests, where the accelerating voltage of 15 kV was kept constant. In total, 21 fatigue experiments were conducted for SLM additive manufactured samples under 700 mm/s, 1000 mm/s and 1300 mm/s laser scanning speed respectively, and experiments for each type of samples

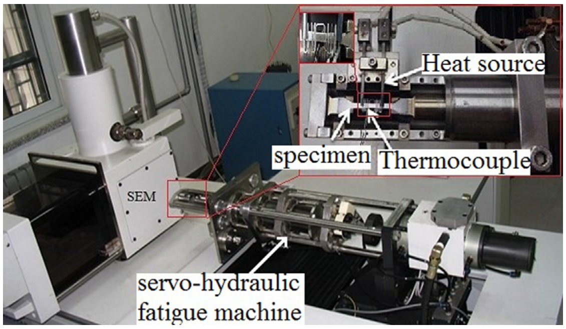

Fig. 3. In-situ high temperature SEM fatigue experiment system.

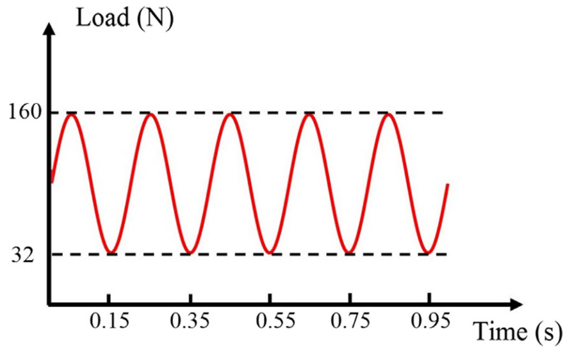

Fig. 4. Tensile fatigue loading loop history.

were performed under 7 increasing temperature points. The relation between fatigue cycle times and temperature is shown in Fig. 5.

3.2. Fatigue performance of SLM additive manufactured Al-Si10-Mg samples at elevated temperature

3.2.1. In-situ observation of fatigue crack initiation and propagation

Fig. 6 shows the micro crack formation and propagation process at different fatigue loading cycles at room temperature (25 °C), where the sample is fabricated at laser scanning speed 700 mm/s, laser power P_L = 370 W, and powder layer thickness 0.03 mm. It can be seen from Fig. 6 that there are some voids and precipitates over the sample surface. As shown in Fig. 6(b), micro crack starts to appear around the U-shape notch location when the fatigue cycle is 14998. With the increase of fatigue cycles, crack propagates rapidly along the main direction perpendicular to the uniaxial loading direction. When the fatigue loading cycle reaches to 17208, the secondary micro crack below the main crack starts to develop and propagate, but the main crack propagation is dominant, and finally the main crack quickly develops into the rupture at loading cycle 17814.

Fig. 7 shows the micro crack formation and propagation process at different fatigue loading cycles at room temperature, where the sample is fabricated at laser scanning speed 1000 mm/s, laser power P_L = 370 W, and powder layer thickness 0.03 mm. Micro crack starts to develop when fatigue loading cycle reaches to 15560, and develops very slowly until loading cycle 40000. Afterwards, the crack propagation speed becomes faster and faster until fracture at loading cycle 61518.

Fig. 8 shows the micro cracks formation and propagation process at different fatigue loading cycles at room temperature, where the sample is fabricated at laser scanning speed 1300 mm/s, laser power P_L = 370 W, and powder layer thickness 0.03 mm. Micro crack starts to initiate at fatigue loading cycle 38836, and develops gradually until fatigue cycle 50814. Afterwards, the main crack meets surface void, another new secondary crack nearby surface void location starts to grow at fatigue cycle 52107, propagates quickly and becomes the new main crack, and finally results in the fracture of the specimen at loading cycle 52304.

Fig. 9 shows the micro crack formation and propagation process at different fatigue loading cycles under elevated temperature 400 °C, where the sample is fabricated at laser scanning speed 700 mm/s, laser power P_L = 370 W, and powder layer thickness 0.03 mm. when the fatigue cycle 500, two main edge micro cracks "A" and "B" start to appear around the U-notch, meanwhile another inner micro crack "C" far away from the U-notch also starts to develop. With the increase of loading cycle, crack "A" develops quickly and becomes the dominant crack, and the crack "B" develops slowly and becomes stable and silent. Meanwhile, the inner

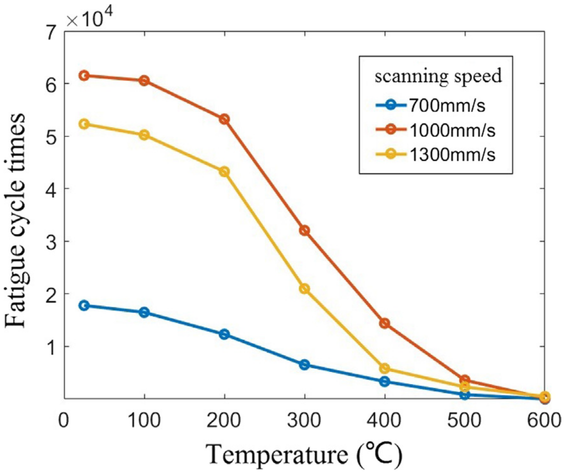

Fig. 5. Relation between fatigue cycle times and the temperature.

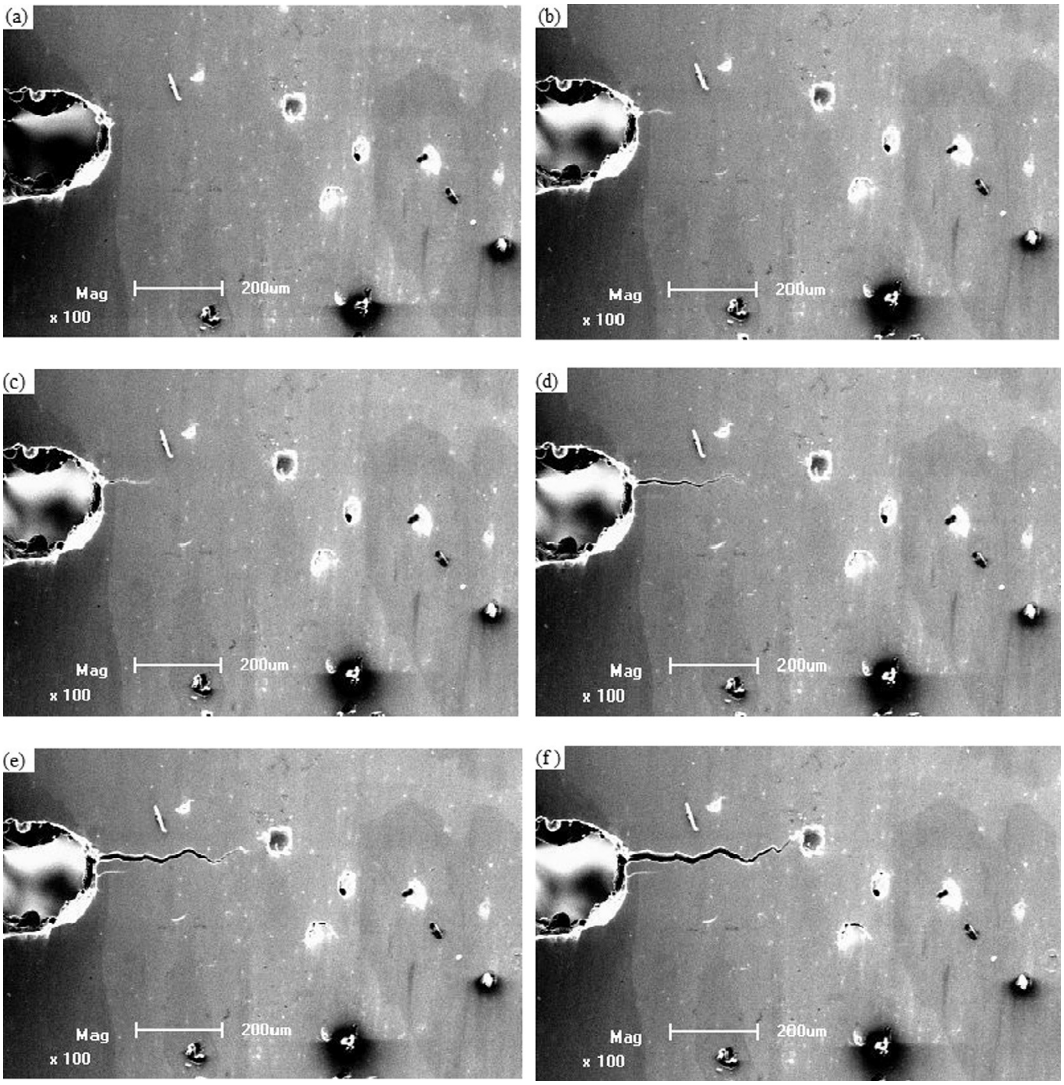

Fig. 6. The fatigue crack propagation process for SLM additive manufactured sample (scanning speed = 700 mm/s) at room temperature: (a) 0; (b) 14998; (c) 16150; (d) 17208; (e) 17531; (f) 17620.

crack “C” grows gradually in length and widen up its gaps. When the number of fatigue loading cycle is 3327, the main crack “A” and the inner crack “C” suddenly penetrate through the medium, and coalescence into one main crack, thus leading to the global failure of the sample at loading cycle 3341.

Fig. 10 shows the micro cracks formation and propagation process at different fatigue loading cycles under elevated temperature 400 °C, where the sample is fabricated at laser scanning speed 1000 mm/s, laser power $P_L = 370$ W, and powder layer thickness 0.03 mm. Micro crack “A” around the U-notch starts to appear when the fatigue loading cycle is 405, and develops very slowly until the number of the fatigue loading cycle is 5600. Then, another new micro crack “B” starts to appear nearby the first micro crack “A”. With the increase of fatigue loading cycle, the new micro crack “B” develops quickly perpendicular to the loading direction, while the first crack stops. Finally, the sample fails until the number of the fatigue loading cycle is 14411.

Fig. 11 shows the micro cracks formation and propagation process at different fatigue loading cycles under elevated temperature 400 °C, where the sample is fabricated at laser scanning speed 1300 mm/s, laser power $P_L = 370$ W, and powder layer thickness 0.03 mm. Micro crack starts to appear at fatigue loading cycle 2007, and propagates stably with the increase of loading cycle. Finally, the sample failures at loading cycle 5812.

In order to quantitatively investigate the effect of temperature and scanning speed on the crack growth rate, the crack lengths at different cycles are counted as shown in Fig. 12. In this figure, the crack growth rate increases fast with the fatigue cycle increasing. Usually, the failure process of the material mainly includes three stages: the initiation of cracks, the stable propagation of cracks and the instantaneous fracture of cracks. The first two processes are defined as the growth phase of the crack. This phase evolves from the starting points of crack growth curve to the points marked as arrows in the Fig. 12. Here we use the ratio of the extended length of the

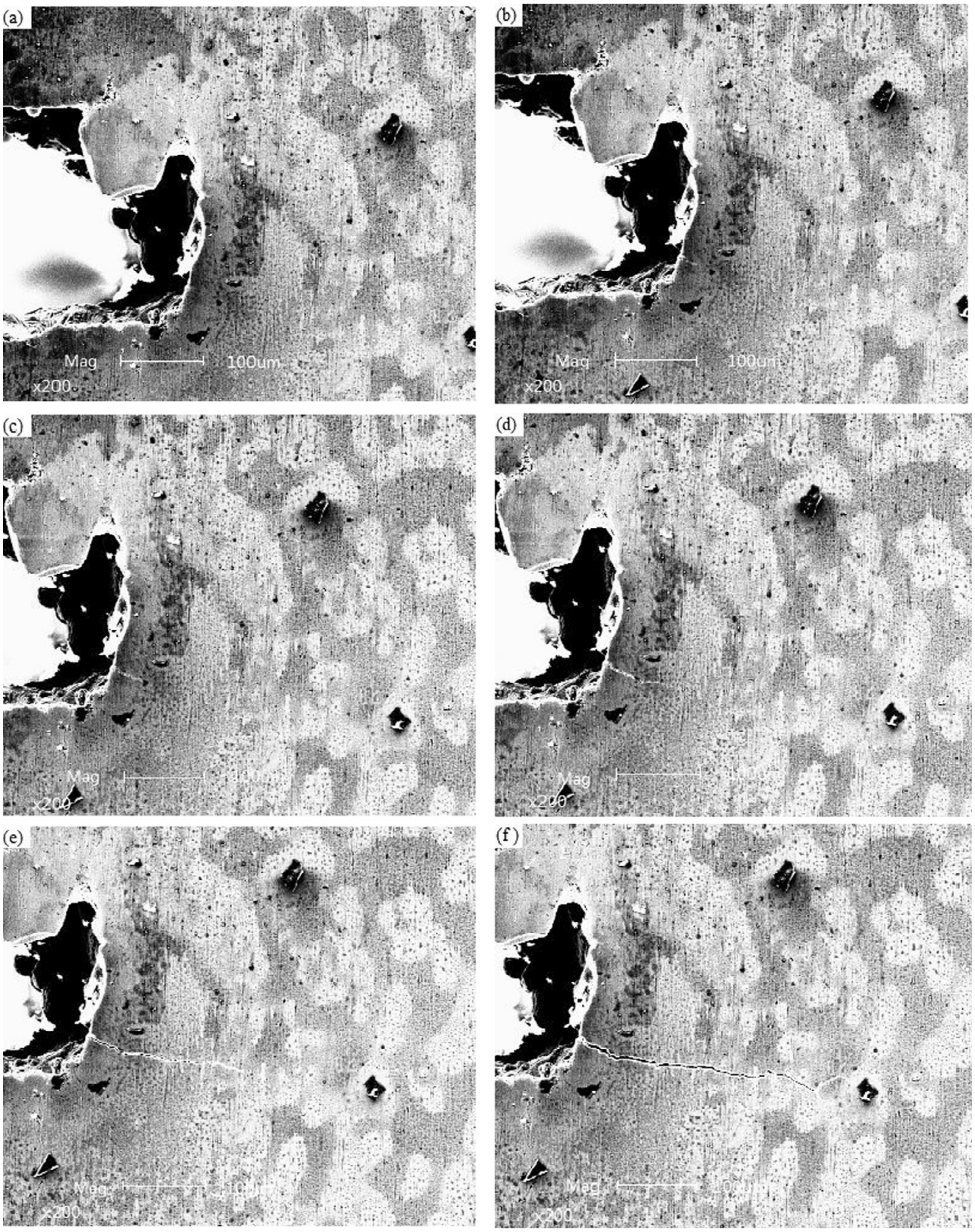

Fig. 7. The fatigue crack propagation process for SLM additive manufactured sample (scanning speed = 1000 mm/s) at room temperature. (a) 0; (b) 15560; (c) 28022; (d) 40000; (e) 52008; (f) 60894.

crack to the fatigue cycle time as the average rate of the crack growth. Therefore, we obtained the crack growth rates of the additive manufactured Al-Si10-Mg alloys at 25 °C are 13.4 nm/cycle, 5.3 nm/cycle and 6.5 nm/cycle for scanning speed of 700 mm/s, 1000 mm/s and 1300 mm/s, respectively. When the temperature is 400 °C, the crack growth rates for different scanning speeds are 41.8 nm/cycle (700 mm/s), 27.2 nm/cycle (1000 mm/s) and 56.9 nm/cycle (1300 mm/s), respectively. We find that the additive manufactured Al-Si10-Mg alloys have the minimum crack growth rate at the scanning speed 1000 mm/s at 25 °C and the crack growth rate of the alloys increases with the increasing temperature for the same scanning speed.

3.2.2. Void features of after-fatigue specimens

Fig. 13 shows the void defect features and spatial distribution within sample harvested after fatigue experiments at room

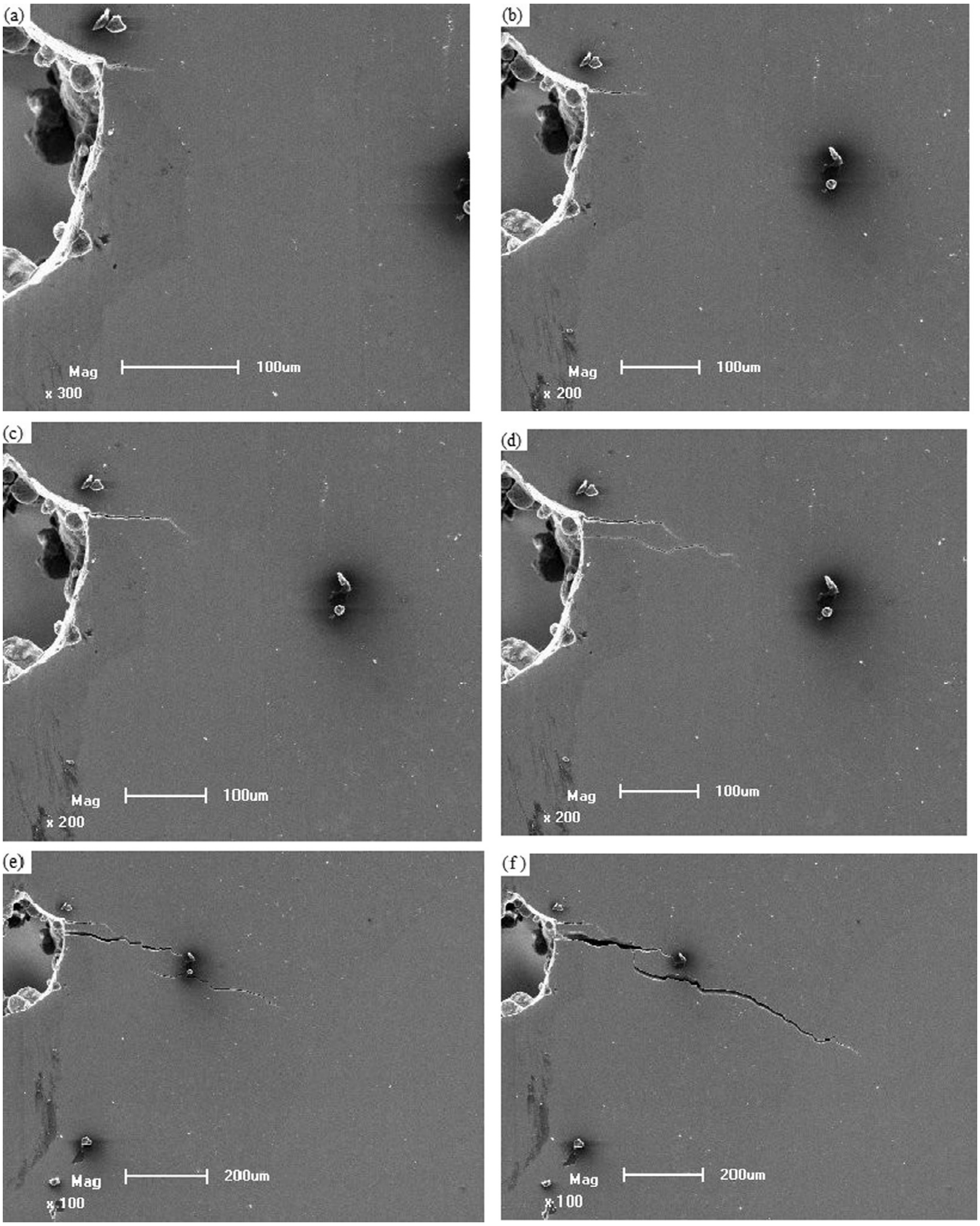

Fig. 8. The fatigue crack propagation process for SLM additive manufactured sample (scanning speed = 1300 mm/s) at room temperature. (a) 38836; (b) 46078; (c) 50027; (d) 50814; (e) 52017; (f) 52211.

temperature, where the sample is fabricated at laser scanning speed 700 mm/s, laser power $P_L = 370$ W, and powder layer thickness 0.03 mm. Fig. 14 shows the void defect features and spatial distribution within sample harvested after fatigue experiments performed at room temperature, where the sample is fabricated at laser scanning speed 1000 mm/s, laser power $P_L = 370$ W, and powder layer thickness 0.03 mm. The fatigue loading cycle is 17,814 for the sample fabricated at laser scanning speed 700 mm/s, which is much lower than the number of the fatigue loading cycle 61,518 for sample fabricated at laser scanning speed 1000 mm/s, also much lower than that of 52,304 for sample fabricated at laser scanning speed 1300 mm/s. It can be seen from Fig. 13 that there are randomly distributed void defects within the sample fabricated at laser scanning speed 700 mm/s, which contribute to the degraded fatigue resistance.

Similar results are checked and confirmed for other samples, and the void percentage before fatigue experiments are shown in

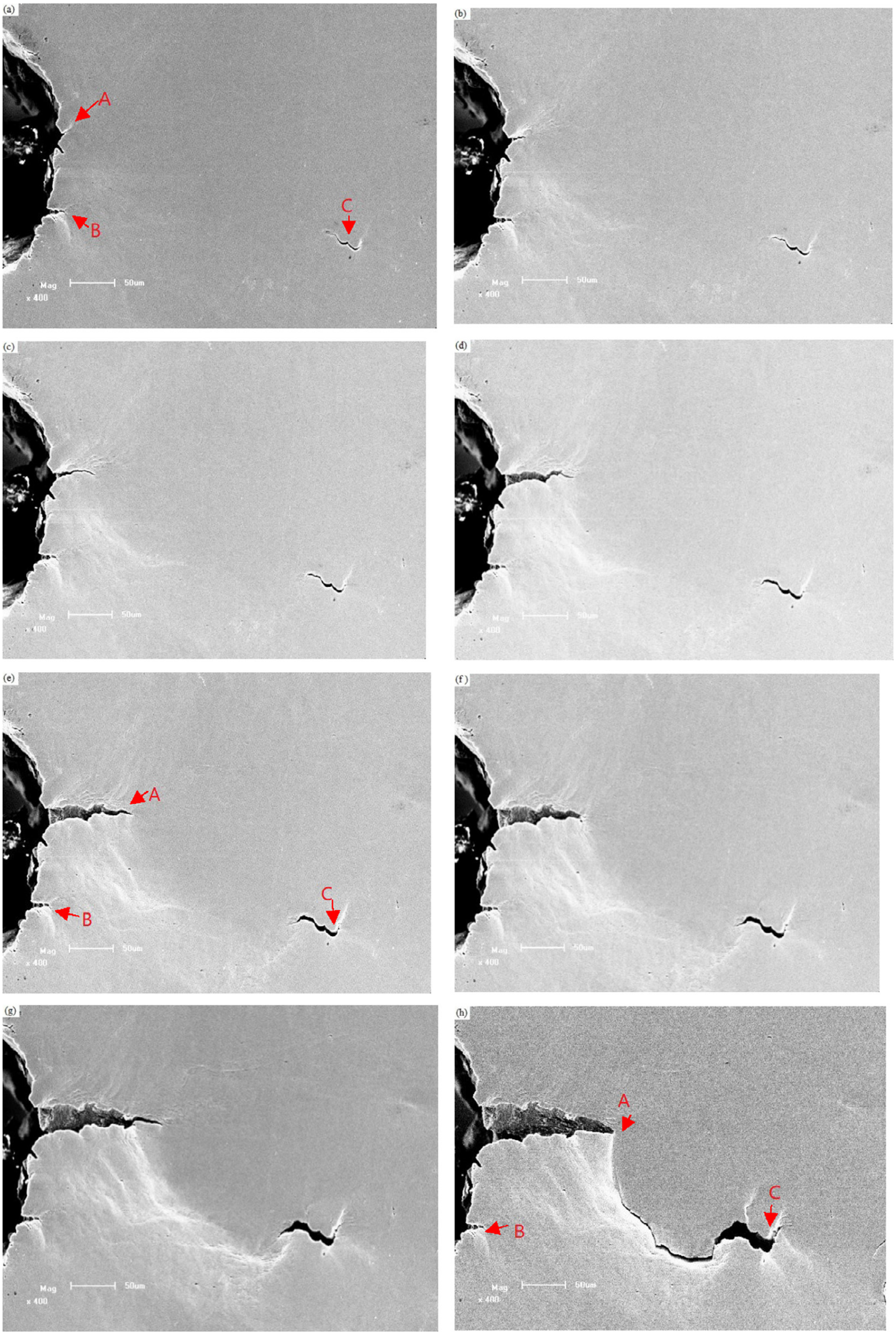

Fig. 9. The fatigue crack propagation process for SLM additive manufactured sample (scanning speed = 700 mm/s) at 400 °C. (a) 500; (b) 1500; (c) 2006; (d) 2602; (e) 2802; (f) 3003; (g) 3204; (h) 3327.

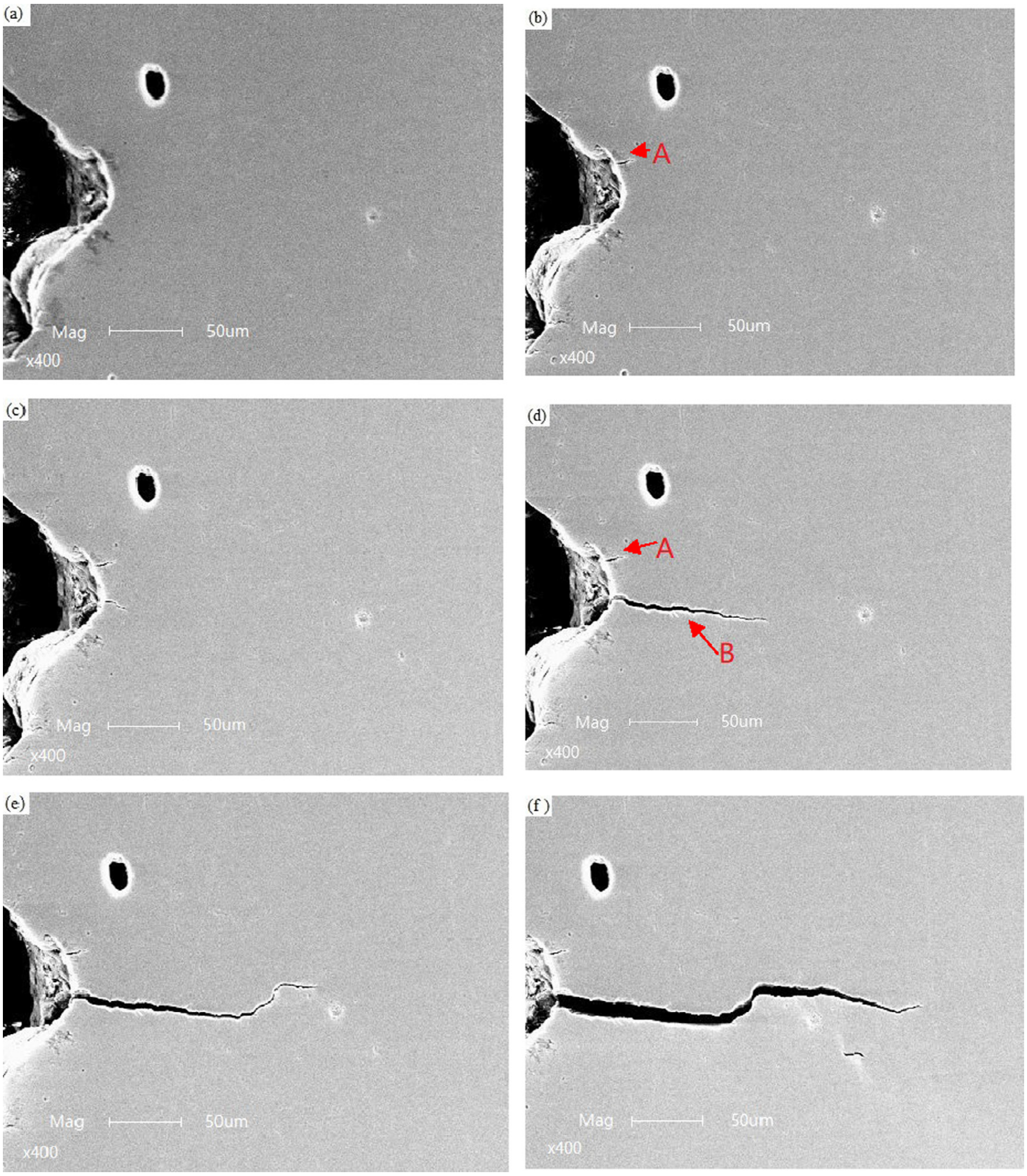

Fig. 10. The fatigue crack propagation process for SLM additive manufactured sample (scanning speed = 1000 mm/s) at 400 °C. (a) 405; (b) 5600; (c) 10008; (d) 12411; (e) 13636; (f) 14001.

Table 2. It can be concluded that there is a strong relation between void defects percentage and fatigue resistance of all samples: with the increase of voids percentage, its fatigue life time drops remarkably.

4. Discussion

When the fatigue samples are constructed with layer-by-layer procedure, the individual lines of material are gradually melted and recrystallized. The melting of metal powder by an energy beam and AM product with reliable mechanical integrity requires reasonable optimization of SLM AM process parameters, such as: laser power, scan speed, thickness of layer, overlap rate and building direction. Voids are apparent throughout the bulk of the Al-Si10-Mg specimens, grown in both directions, but they appear more numerous in the materials grown in the vertical orientation. Porosity is a common defect in metal AM parts and results in degradation of the mechanical properties. Porosity can be powder-induced, process-induced or an artifact of solidification. (1) Powder-induced porosity, gas pores may form inside the powder feedstock during powder melting process, and these pre-existing spherical gas pores can be transferred into the as-fabricated samples; (2) Process-induced porosity is dominant, and pores are formed when the applied

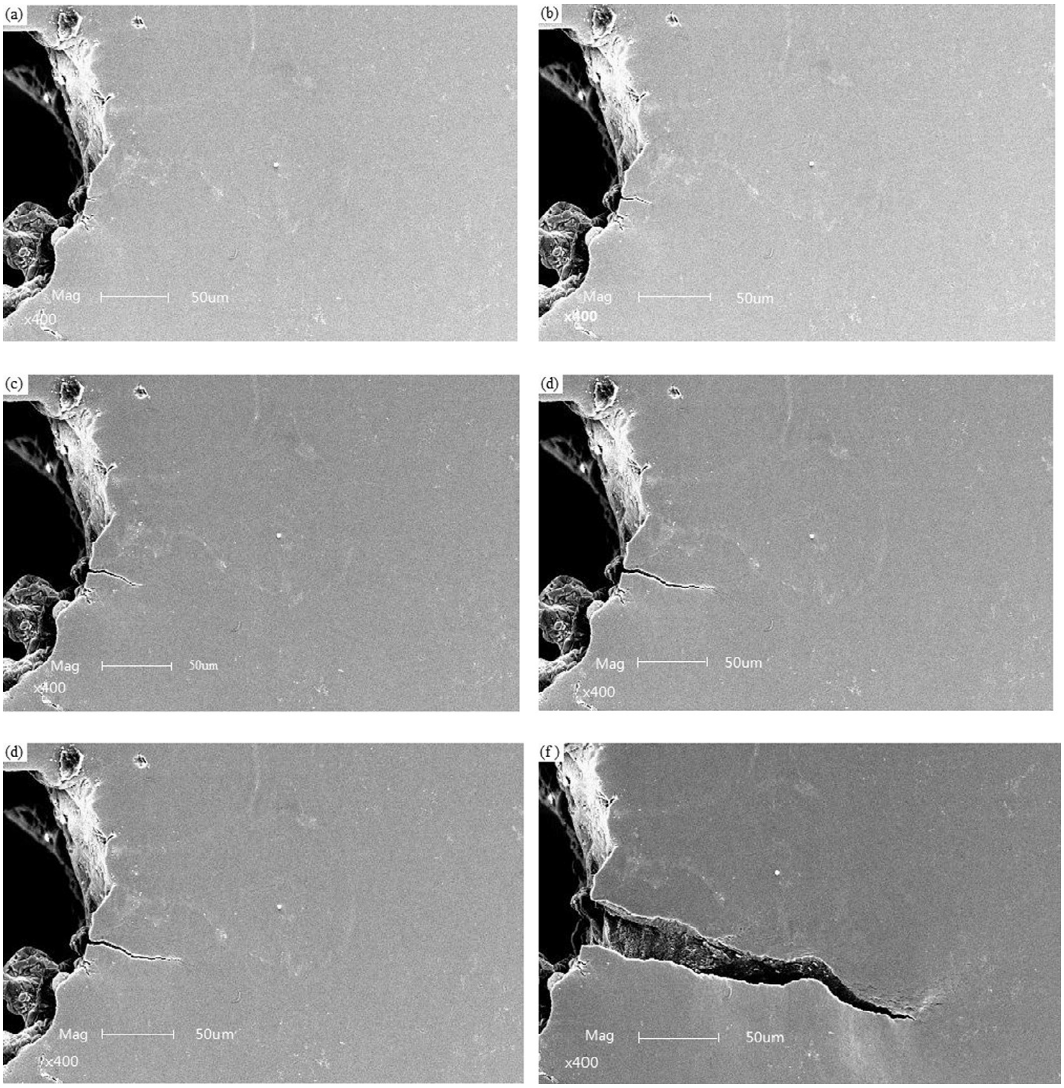

Fig. 11. The fatigue crack propagation process for SLM additive manufactured sample (scanning speed = 1300 mm/s) at 400 °C. (a) 2007; (b) 2477; (c) 2802; (d) 3209; (e) 4404; (f) 5679.

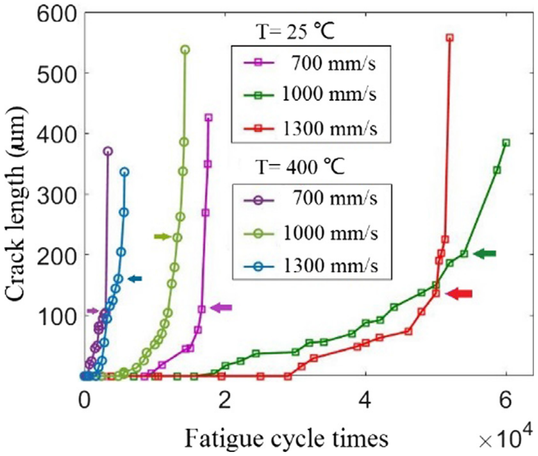

Fig. 12. The relationship between crack length and fatigue cycle times in the different temperature and scanning speed.

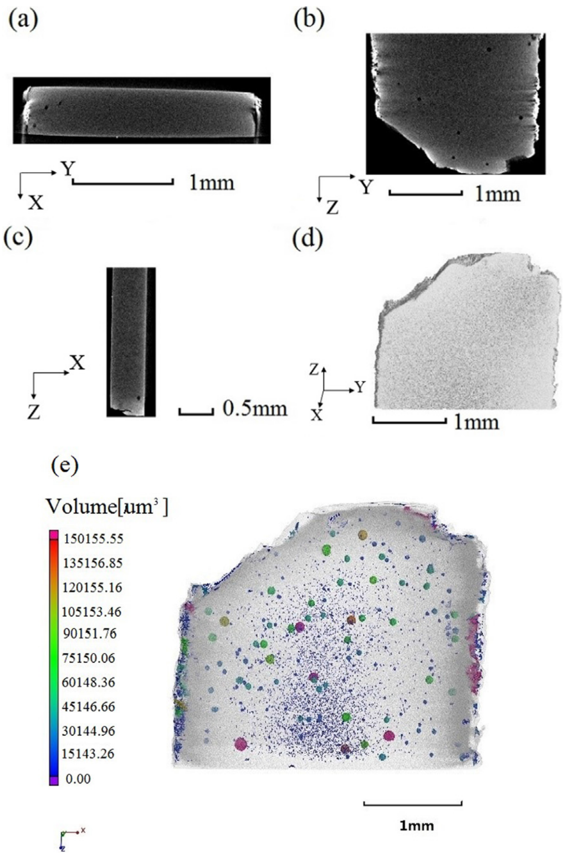

Fig. 13. Microstructure and voids distribution of as fabricated sample after fatigue test (scanning speed 700 mm/s, 25 °C) (a) Z-direction tomogram; (b) X-direction tomogram; (c) Y-direction tomogram; (d) three-dimensional CT tomogram; (e) voids distribution of the sample.

energy is not sufficient for complete melting or spatter ejection occurs. These pores are typically non-spherical, and come in a variety of sizes (sub-micron to macroscopic). When there is not enough power to supply to a region of powder, lack of fusion can occur and un-melted powder particles can be formed in or near the pore. When the applied power is too high, spatter ejection may occur in a process known as keyhole formation. Process-induced porosity has other contributors, including the effect of powder consolidation from a loosely packed powder bed to a fully dense part. Shrinkage porosity is the incomplete flow of metal into the desired melt region [45,51].

During the SLM additive manufacturing process, the scanning energy input is determined with scanning speed, hatch distance, and layer thickness as well as the preheating of the platform. The variation of the energy input is conducted by varying the scanning speed at 700 mm/s, 1000 mm/s and 1300 mm/s. Following Eq. (1) is employed to calculate the resulting energy input:

$$E_V = \frac{P_L}{v_s \Delta y_s D_s} \tag{1}$$

The EOS M290 machine parameters employed in the current investigation are shown in Table 3, fatigue properties may be influenced by surface finish and porosity, and these top biggest voids are mainly responsible for the degradation of fatigue mechanical performances. Fig. 15 shows the relationship between scanning speed and porosity rate. With the increase of scanning speed from 700 mm/s to 1000 mm/s, the porosity ratio and pore size within the fatigue samples decrease remarkably, and the spatial distribution of dominant top largest voids are inhomogeneous, resulting in the remarkable increase of fatigue performance. When the scanning speed is higher than 1000 mm/s, E_V decreases and results in increase of porosity due to lack of fusion and un-melted powder particles formed in or near the pore. Thus, slight increase of porosity at scanning speed 1300 mm/s can be confirmed with micro-CT characterization, and result in slight decrease of fatigue behaviors.

5. Conclusion

SLM additive manufactured Al-Si10-Mg fatigue samples are fabricated and in-situ fatigue experiments of are carried out under SEM environment at 25 °C, 100 °C, 200 °C, 300 °C, 400 °C, 500 °C and 600 °C, respectively. The fatigue mechanical behaviors, microstructure evolution and crack propagations of as-fabricated Al-Si10-Mg samples are characterized. Micro-CT tomography 3D

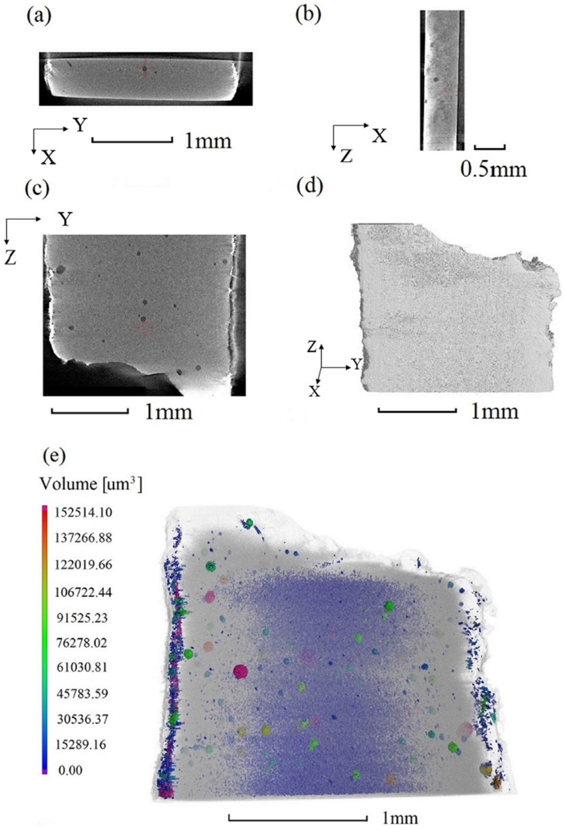

Fig. 14. Microstructure and voids distribution of as fabricated sample after fatigue test (scanning speed 1000 mm/s, 25 °C) (a) Z-direction tomogram; (b) Y-direction tomogram; (c) X-direction tomogram; (d) three-dimensional CT tomogram; (e) voids distribution of the sample.

Table 3
SLM process parameters employed for the fabrication.

Laser power P_L [W]	Laser spot diameter [mm]	Laser profile	Hatch distance Δy_s [mm]	Layer thickness D_s [mm]	Preheat temperature [°C]	Scanning speed v_s [mm/s]
370	0.20	Gaussian	0.08	0.03	220	700, 1000, 1300

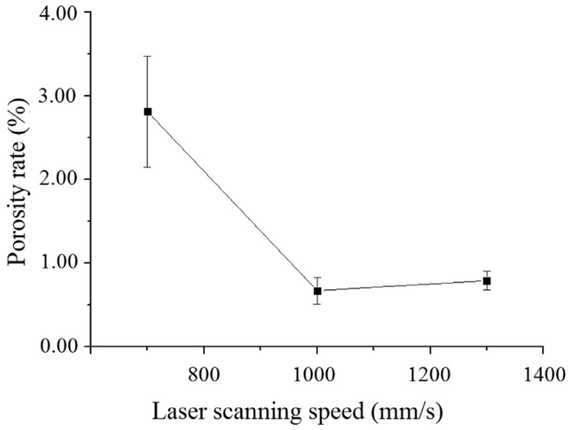

Fig. 15. The relationship between laser scanning speed and porosity rate.

imaging techniques are employed for exploring the link between SLM defects and fatigue performances.

(1) The fatigue performance of samples fabricated with scanning speed of 1000 mm/s is better than samples fabricated with scanning speed of 700 mm/s and 1300 mm/s, respectively.
(2) With the increase of the temperature, the fatigue life of samples fabricated with scanning speed of 1000 mm/s and 1300 mm/s drops gradually until the temperature reaches to 200 °C. Afterwards, the fatigue life time drops remarkably when temperature is above 250 °C. For samples fabricated with scanning speed of 700 mm/s, the life time drops smoothly with the increase of the temperature at all temperature points. Regarding the effect of porosity and temperature on fatigue life, it can be seen that the effect of porosity is more pronounced at low temperatures, while the effect of temperature is dominant when the temperature is greater than 400 °C.
(3) Micro-CT confirms that there is a strong relation between void defect percentage and fatigue resistance of all samples. With the increase of void percentage, its fatigue life time drops remarkably.

Acknowledgments

This research is supported by the National Natural Science Foundation of China under Grant No. 11702023, No. 11632010 and No. 11872035.

References

[1] Khairallah SA, Anderson AT, Rubenchik A, King WE. Laser powder-bed fusion additive manufacturing: Physics of complex melt flow and formation mechanisms of pores, spatter, and denudation zones. Acta Mater 2016;108:36–45. https://doi.org/10.1016/j.actamat.2016.02.014.
[2] Townsend A, Senin N, Blunt L, Leach RK, Taylor JL. Surface texture metrology for metal additive manufacturing: a review. Precis Eng 2016;46:34–47. https://doi.org/10.1016/j.precisioneng.2016.06.001.
[3] Yadollahi A, Shamsaei N. Additive manufacturing of fatigue resistant materials: Challenges and opportunities. Int J Fatigue 2017;98:14–31. https://doi.org/10.1016/j.ijfatigue.2017.01.001.
[4] Zhibo L, Yaoyao Z. A survey of finite element analysis of temperature and thermal stress fields in powder bed fusion additive manufacturing. Addit Manuf 2018;21:318–32. https://doi.org/10.1016/j.addma.2018.03.022.
[5] Noriko R, Wei W, Khamis E, Attallah MM. Selective laser melting of AlSi10Mg alloy: Process optimisation and mechanical properties development. Mater Des 2015;65:417–24. https://doi.org/10.1016/j.matdes.2014.09.044.
[6] Buchbinder D, Schleifenbaum H, Heidrich S, Meiners W, Bültmann J. High power selective laser melting (HP SLM) of aluminum parts. Phys Procedia 2011;12:271–8. https://doi.org/10.1016/j.phpro.2011.03.035.
[7] Maamoun AH, Elbestawi M, Dosbaeva GK, Veldhuis SC. Thermal post-processing of AlSi10Mg parts produced by selective laser melting using recycled powder. Addit Manuf 2018;21:234–47. https://doi.org/10.1016/j.addma.2018.03.014.
[8] Brandl E, Heckenberger U, Holzinger V, Buchbinder D. Additive manufactured AlSi10Mg samples using Selective Laser Melting (SLM): Microstructure, high cycle fatigue, and fracture behavior. Mater Des 2012;34:159–69. https://doi.org/10.1016/j.matdes.2011.07.067.
[9] Bagherifard S, Beretta N, Monti S, Riccio M, Bandini M, Guagliano M. On the fatigue strength enhancement of additive manufactured AlSi10Mg parts by mechanical and thermal post-processing. Mater Des 2018;145:28–41. https://doi.org/10.1016/j.matdes.2018.02.055.
[10] Aboulkhair NT, Maskery L, Tuck C, Ashcroft L, Everitt NM. Improving the fatigue behaviour of a selectively laser melted aluminium alloy: Influence of heat treatment and surface quality. Mater Des. 2016;104:174–82. https://doi.org/10.1016/j.matdes.2016.05.041.
[11] Brandao AD, Gumpinger J, Gschweitl M, Seyfert C, Hofbauer P, Ghidini T. Fatigue Properties of additively manufactured AlSi10Mg-Surface treatment effect. Procedia Struct Integrity 2017;7:58–66. https://doi.org/10.1016/j.prostr.2017.11.061.
[12] Zhang BC, Lee XH, Bai JM, Guo JF, Wang P, Sun CN, et al. Study of selective laser melting (SLM) Inconel 718 part surface improvement by electrochemical polishing. Mater Des 2016;116:531–7. https://doi.org/10.1016/j.matdes.2016.11.103.
[13] Shi QW, Roux S, Latourte F, Hild F, Loisnard D, Brynaert N. On the use of SEM correlative tools for in situ mechanical tests. Ultramicroscopy 2018;184:71–87. https://doi.org/10.1016/j.ultramic.2017.08.005.
[14] Han QN, Qiu WH, Shang YB, Shi HJ. In-situ SEM observation and crystal plasticity finite element simulation of fretting fatigue crack formation in Ni-base single-crystal superalloys. Tribol Int 2016;10:33–42. https://doi.org/10.1016/j.triboint.2016.03.025.
[15] Ma XF, Shi HJ. In situ SEM studies of the low cycle fatigue behavior of DZ4 superalloy at elevated temperature: Effect of partial recrystallization. Int J Fatigue 2014;61:255–63. https://doi.org/10.1016/j.ijfatigue.2013.11.001.
[16] Liang JC, Wang Z, Xie HF, Li XD. In situ scanning electron microscopy-based high-temperature deformation measurement of nickel-based single crystal superalloy up to 800 °C. Opt Laser Eng 2018;108:1–14. https://doi.org/10.1016/j.optlaseng.2018.04.016.
[17] Zhang YY, Shi HJ, Gu JL, Li CP, Kadau K, Luesebrink O. Crystallographic analysis for fatigue small crack growth behaviors of a nickel-based single crystal by in situ SEM observation. Theo Appl Fract Mech 2014;69:80–9. https://doi.org/10.1016/j.tafmec.2013.11.002.
[18] Zhang JZ, He XD, Tang H, Du SY. Direct high resolution in situ SEM observations of small fatigue crack opening profiles in the ultra-fine grain aluminium alloy. Mater Sci and Eng, A 2008;485:115–8. https://doi.org/10.1016/j.msea.2007.08.006.
[19] Jiang R, Pierron F, Octaviani S, Reed PAS. Characterisation of strain localisation processes during fatigue crack initiation and early crack propagation by SEM-DIC in an advanced disc alloy. Mater Sci Eng, A 2017;699:128–44. https://doi.org/10.1016/j.msea.2017.05.091.
[20] Li WP, Wang XG, Liu B, Fang QH, Jiang C. Fracture mechanisms of a Mo alloyed CoCrFeNi high entropy alloy: In-situ SEM investigation. Mater Sci Eng, A 2018;723:79–88. https://doi.org/10.1016/j.msea.2018.03.032.
[21] Tan CS, Sun QY, Xiao L, Zhao YQ, Sun J. Characterization of deformation in primary α phase and crack initiation and propagation of TC21 alloy using in-situ SEM experiments. Mater Sci Eng, A 2018;725:33–42. https://doi.org/10.1016/j.msea.2018.03.123.
[22] Lavenstein S, Crawford B, Sim GD, Shade PA, Woodward C, El-Awady JA. High frequency in situ fatigue response of Ni-base superalloy Rene-N5 microcrystals. Acta Mater 2018;144:154–63. https://doi.org/10.1016/j.actamat.2017.10.049.
[23] Chai GC, Peng RL, Johansson S. Fatigue behaviors in duplex stainless steel studied using in-situ SEM/EBSD method. Procedia Mater Sci 2014;3:1748–53. https://doi.org/10.1016/j.mspro.2014.06.282.
[24] Yan L, Fan JK. In-situ SEM study of fatigue crack initiation and propagation behavior in 2524 aluminum alloy. Mater Des 2016;110:592–601. https://doi.org/10.1016/j.matdes.2016.08.004.
[25] Zhang W, Liu YM. Investigation of incremental fatigue crack growth mechanisms using in situ SEM testing. Int J Fatigue 2011;42:14–23. https://doi.org/10.1016/j.ijfatigue.2011.03.004.
[26] Zhu ML, Xuan FZ, Tu ST. Observation and modeling of physically short fatigue crack closure in terms of in-situ SEM fatigue test. Mater Sci Eng, A 2014;618:86–95. https://doi.org/10.1016/j.msea.2014.08.021.
[27] Liao D, Zhu SP, Correia JA, Jesus AM, Calçada R. Computational framework for multiaxial fatigue life prediction of compressor discs considering notch effects.

Eng Frac Mech 2018;202:423–35. https://doi.org/10.1016/j.engfracmech.2018.08.009.

[28] Zhu SP, Liu Q, Peng WW, Zhang XC. Computational-experimental approaches for fatigue reliability assessment of turbine bladed disks. Int J Mech Sci 2018;142:502–17. https://doi.org/10.1016/j.ijmecsci.2018.04.050.

[29] Zhu SP, Foletti S, Beretta S. Evaluation of size effect on strain-controlled fatigue behavior of a quench and tempered rotor steel: experimental and numerical study. Mater Sci Eng, A 2018;735:423–35. https://doi.org/10.1016/j.msea.2018.08.073.

[30] Zhu SP, Yu ZY, Liu Q, Ince A. Strain energy-based multiaxial fatigue life prediction under normal-shear stress interaction. Int J Damage Mech 2018:1–32. https://doi.org/10.1177/1056789518786031.

[31] Zhu SP, L YH, Liu Q, Yu ZY. Strain energy gradient-based LCF life prediction of turbine discs using critical distance concept. Int J Fatigue 2018;113:33–42. https://doi.org/10.1016/j.ijfatigue.2018.04.006.

[32] Wang RZ, Zhu SP, Wang J, Zhang XC, Tu ST, Zhang CC. High temperature fatigue and creep-fatigue behaviors in a Ni-based superalloy: Damage mechanisms and life assessment. Int J Fatigue 2019;118:8–21. https://doi.org/10.1016/j.ijfatigue.2018.05.008.

[33] Qian G, Lei WS, Niffenegger M, Gonzalez-Albuixech VF. On the temperature independence of statistical model parameters for cleavage fracture in ferritic steels. Phil Mag 2018;98:959–1004. https://doi.org/10.1080/14786435.2018.1425011.

[34] Qian G, Cao YP, Niffenegger M, Chao YJ, Wu WW. Comparison of constraint analyses with global and local approaches under uniaxial and biaxial loadings. Eur J Mech A-Solid 2018;69:135–46. https://doi.org/10.1016/j.euromechsol.2017.12.006.

[35] Qian G, Lei W-S, Peng L, Yu Z, Niffenegger M. Statistical assessment of notch toughness against cleavage fracture of ferritic steels. Fatigue Fract Eng Mater Struct 2018;41(5):1120–31. https://doi.org/10.1111/ffe.v41.510.1111/ffe.12756.

[36] Qian GA, Niffenegger M, Sharabi M, Lafferty N. Effect of non-uniform reactor cooling on fracture and constraint of a reactor pressure vessel. Fatigue FracEng Mater Struct 2018;41:1559–75. https://doi.org/10.1111/ffe.12796.

[37] Qian G, Zhai J, Yu Z, Lei WS, Wu W. Non-proportional size scaling of strength of concrete in uniaxial and biaxial loading conditions. Fatigue Frac Eng Mater Struct 2018;41:1733–45. https://doi.org/10.1111/ffe.12813.

[38] Thompson A, Maskery I, Leach RK. X-ray computed tomography for additive manufacturing: a review 072001 Meas Sci Technol 2016;27http://iopscience.iop.org/article/10.1088/0957-0233/27/7/072001/meta.

[39] Kruth JP, Bartscher M, Carmignato S, Schmitt R, De Chiffre L, Weckenmann A. Computed tomography for dimensional metrology. CIRP Ann Manuf Technol 2011;60:821–42.

[40] De Chiffre L, Carmignato S, Kruth JP, Schmitt R, Weckenmann A. Industrial applications of computed tomography. CIRP Ann Manuf Technol 2014;63:655–77.

[41] Plessis AD, Sperling P, Beerlink A, Tshabalala L, Hoosain S, Mathe N, le Roux SG. X-ray microcomputed tomography in additive manufacturing: a review of the current technology and applications. 3D Print Addit Manuf 2018;5:227–47. https://doi.org/10.1089/3dp.2018.0060.

[42] Yadroitsev I, Yadroitsava I, Bertrand P, et al. Factor analysis of selective laser melting process parameters and geometrical characteristics of synthesized single tracks. Rapid Prototyping J 2012;18:201–8. https://doi.org/10.1108/13552541211218117.

[43] Matilainen VP, Piili H, Nyrhila O. Preliminary investigation of keyhole phenomena during single layer fabrication in laser additive manufacturing of stainless steel. Phys Procedia 2015;78:377–87. https://doi.org/10.1016/j.phpro.2015.11.052.

[44] Buchbinder D, Schleifenbaum H, Heidrich S, et al. High power selective laser melting (HP SLM) of aluminum parts. Phys Procedia 2011;12:271–8. https://doi.org/10.1016/j.phpro.2011.03.035.

[45] Kasperovich G, Haubrich J, Gussone J, Requena G. Correlation between porosity and processing parameters in TiAl6V4 produced by selective laser melting. Mater Des 2016;105:160–70. https://doi.org/10.1016/j.matdes.2016.05.070.

[46] King WE, Barth HD, Castillo VM, et al. Observation of keyhole-mode laser melting in laser powder-bed fusion additive manufacturing. J Mater Process Technol 2014;214:2915–25. https://doi.org/10.1016/j.jmatprotec.2014.06.005.

[47] Aboulkhair NT, Everitt NM, Ashcroft I, et al. Reducing porosity in AlSi10Mg parts processed by selective laser melting. Addit Manuf 2014;1–4:77–86. https://doi.org/10.1016/j.addma.2014.08.001.

[48] Plessis AD, le Roux SG. Standardized X-ray tomography testing of additively manufactured parts: A round robin test. Addit Manuf 2018;24:125–36. https://doi.org/10.1016/j.addma.2018.09.014.

[49] Plessis AD, Sperling P, Beerlink A, Tshabalala L, Hoosain S, Mathe N, et al. Standard method for micro CT-based additive manufacturing quality control 2: Density measurement. Methods X 2018;5:1117–23https://doi:10.1016/j.mex.2018.09.006.

[50] Tammas WS, Withers PJ, Todd I, Prangnell PB. The influence of porosity on fatigue crack initiation in additively manufactured titanium components. Sci Rep 2017;7:1–13. https://doi.org/10.1038/s41598-017-06504-5.

[51] Mower TM, Long MJ. Mechanical behavior of additive manufactured, powder-bed laser-fused materials. Mater Sci Eng A 2016;651:198–213. https://doi.org/10.1038/s41598-017-06504-5.